

The mass-morphology relation of TNG50 galaxies

Bruno M. Celiz^{1,2,3,*}, Julio F. Navarro⁴, Mario G. Abadi^{2,3}, and Volker Springel⁵

¹ Facultad de Matemática, Astronomía, Física y Computación, UNC, Medina Allende s/n, X5000HUA, Córdoba, Argentina

² Instituto de Astronomía Teórica y Experimental, CONICET-UNC, Laprida 854, X5000BGR, Córdoba, Argentina

³ Observatorio Astronómico de Córdoba, UNC, Laprida 854, X5000BGR, Córdoba, Argentina

⁴ Department of Physics and Astronomy, University of Victoria, Victoria, BC, V8P 5C2, Canada

⁵ Max-Planck-Institut für Astrophysik, Karl-Schwarzschild-Straße 1, D-85741 Garching, Germany

Received XXX; accepted YYY

ABSTRACT

We use the cosmological hydrodynamical simulation TNG50 to study the galaxy mass-morphology relation, as measured by the rotational support of the stellar component of simulated galaxies. For isolated galaxies with stellar mass in the range $8 < \log(M_*/M_\odot) < 11$, rotational support increases with M_* , from dispersion-supported spheroidal dwarfs to massive galaxies with prominent rotationally supported discs. Our results indicate that this correlation arises from the spatial distribution of star formation in TNG50 galaxies, which occurs primarily in two distinct regions: an unresolved, non-rotating central baryonic clump ($r \lesssim 1$ kpc) and a rotationally supported outer disc, separated by a quiescent region. The importance of the inner clump increases with decreasing M_* ; it makes up fewer than 20% of all stars in the most massive galaxies, but more than 80% in dwarfs. This explains why dwarfs have less rotational support than massive galaxies, as well as why all dwarfs have similar stellar half-mass radii, regardless of M_* . It also explains why massive galaxies in TNG50 appear to form inside-out (as the outer disc grows), whereas dwarfs form outside-in, as star formation in the dominant inner clump moves progressively inward. The clump-disc segregation of star formation in TNG50 galaxies is probably numerical in origin. Inner clumps are formed by the accumulation of low-angular momentum gas supported by the equation of state introduced to prevent artificial fragmentation. The decoupled-wind feedback implementation in TNG50 helps to preserve the clumps but disrupts disc formation in its immediate surroundings. This hinders the formation of discs in (dwarf) galaxies whose sizes are not substantially larger than the clump, but has little effect on the larger discs of more massive systems. Our results argue for caution when interpreting the dependence on stellar mass of TNG50 galaxy morphologies, or the evolution of galaxy sizes, especially at the dwarf end.

Key words. galaxies: dwarf – galaxies: kinematics and dynamics – galaxies: star formation

1. Introduction

Galaxy surveys like SDSS¹ (York et al. 2000) and GAMA² (Driver et al. 2011) have shown that low-mass galaxies dominate by number the galaxy population (Kauffmann et al. 2003; Blanton et al. 2005; Li & White 2009; Baldry et al. 2012). Due to their low luminosity, studies of dwarf galaxies (defined as those with $\log(M_*/M_\odot) < 9$) are generally limited to nearby regions, such as the Local Volume or the Local Group of galaxies (see e.g. Mateo 1998; Walter et al. 2008; Swaters et al. 2009; McConnachie 2012; McNichols et al. 2016).

Existing studies of dwarf galaxy morphology show that most dwarfs are irregular, with few examples of pure disc or spheroidal morphologies (see e.g. Karachentsev et al. 2013; Klypin et al. 2015). For example, Moffett et al. (2016) report that irregular galaxies outnumber disc-like galaxies in the mass range $\log(M_*/M_\odot) \lesssim 9.3$ with the difference increasing at lower masses (see van den Bosch & Swaters 2001; Swaters et al. 2009, for a study on late-type dwarf galaxies). Klypin et al. (2015), on the other hand, report that only $\sim 10\%$ of bright dwarf galaxies are spheroids.

The physical processes driving the morphological diversity of dwarf galaxies are not fully understood. Low-luminosity sys-

tems are expected to form in the shallow potential wells of low-mass dark matter halos (see e.g. Moster et al. 2013; Adams et al. 2014; Oh et al. 2015; McNichols et al. 2016; Behroozi et al. 2019; Oman et al. 2019). This implies that the impact of baryonic processes like stellar feedback is enhanced in dwarfs (see e.g. McQuinn et al. 2019; Gutcke et al. 2021; Ostriker & Kim 2022), with possibly strong effects on galaxy morphology. Dwarf galaxies thus provide an ideal testbed for models of star formation and evolution which aim to track the baryon cycle and its impact on galaxy formation and evolution (see e.g. Dekel & Woo 2003; Ferrarotti & Gail 2006; Christensen et al. 2016; El-Badry et al. 2017).

Direct numerical simulations have also struggled to consistently reproduce the diverse morphologies of dwarf galaxies observed in the Local Volume, a "weak tension" regarding our understanding of dwarf galaxy evolution in the prevailing Λ CDM cosmological model (Sales et al. 2022). Key to resolving this tension is the study of the spatially resolved star formation activity in dwarfs, which differ from massive galaxies not only in their morphology, but also in the radial gradients of their stellar populations.

Massive disc galaxies, for example, tend to form *inside-out*, as later accreting material settles in the outer disc because of its higher angular momentum content. Conversely, dwarf galaxies typically exhibit positive radial stellar age gradients, with their youngest and most metal-rich stars inhabiting preferentially the

* e-mail: bruno.celiz@mi.unc.edu.ar

¹ <https://www.sdss.org/>

² <https://www.gama-survey.org/>

inner regions while the oldest populate the outskirts (see e.g. Benítez-Llambay et al. 2016; Albers et al. 2019; Cheng et al. 2024; Fu et al. 2024; Riggs et al. 2024; Tau et al. 2024). How these differences in age gradients between dwarf and luminous galaxies arise is still unclear, but the morphological differences hint at the important role that rotational support may play in the process. Indeed, rotational support seems absent in the stellar components of the faintest galaxies known, the dwarf spheroidal companions of the Milky Way and Andromeda galaxies (see e.g. McConnachie 2012).

Why does rotational support play a diminished role in the stellar component of dwarfs? Is it because gaseous discs do not get established in these systems before stars form in earnest, or is it because the feedback effects of star formation itself act to disrupt thin, rotationally-supported structures in the shallow potential wells of low-mass halos? Or is it perhaps the result of more complex, external effects such as the role of the environment through tidal or ram-pressure stripping, or galaxy mergers?

We use here a state-of-the-art hydrodynamic cosmological simulation (TNG50, Nelson et al. 2019a; Pillepich et al. 2019) to investigate these issues. In particular, we aim to study how the rotational support of the stellar component depends on galaxy mass. We also look into how the spatial distribution of star formation drives the evolution of galaxy size and morphology of isolated galaxies, with the aim of understanding the physical origin of such trends.

This paper is organized as follows: in Section 2 we present details of the simulation used and of the galaxy sample studied. We also introduce the definition of galaxy rotational support adopted throughout this work. In Section 3 we analyse the spatially resolved morphology of isolated galaxies of different mass, and use them to motivate and interpret the observed trends between galaxy mass, size, and rotational support, as well as the evolution of galaxy sizes. Finally, in Section 4 we summarize our results and present our conclusions.

2. Methods

2.1. Simulation

We use for this study The Next Generation Illustris simulations (IllustrisTNG³, Marinacci et al. 2018; Naiman et al. 2018; Pillepich et al. 2018a; Springel et al. 2018; Nelson et al. 2019b), a suite of magneto-hydrodynamic cosmological simulations of a standard Λ CDM Universe ($h = 0.6774$; $\Omega_m = 0.3089$; $\sigma_8 = 0.8159$, consistent with Planck Collaboration et al. 2016). From initial conditions set at redshift $z = 127$, the simulations are evolved with the moving mesh code AREPO (Springel 2010; Pakmor et al. 2016) forward in time until $z = 0$, and the properties of dark matter and baryon particles are systematically recorded in 100 snapshots at intervals of ~ 0.15 Gyr.

Our analysis focuses on simulated galaxies identified in the TNG50-1 run (Nelson et al. 2019a; Pillepich et al. 2019, TNG50 hereafter), a 51.7 Mpc side periodic box containing 2160^3 particles of dark matter of mass $m_{\text{DM}} = 4.5 \times 10^5 M_\odot$, an equal number of initial gas cells, with a “target baryon mass” of $m_{\text{baryon}} = 8.5 \times 10^4 M_\odot$. The Plummer-equivalent gravitational softening for DM and stars is $\epsilon_{\text{DM},*} = 0.29$ kpc and the minimum value of the adaptive gas gravitational softening is $\epsilon_{\text{gas}} = 0.07$ kpc (at redshift $z = 0$).

The baryonic treatment included in TNG50 (updated from the previous Illustris project, Vogelsberger et al. 2013, 2014;

Weinberger et al. 2017; Pillepich et al. 2018a) allows the gas to cool down to a temperature $T = 10^4$ K following the cooling and heating rates computed from local density, redshift and metallicity. The gas above density $n = 0.13 \text{ cm}^{-3}$ is modelled using an effective equation of state to describe a dual-phase interstellar medium gas which prevents artificial fragmentation (Springel & Hernquist 2003). Star formation occurs in gas cells above this density threshold. Stellar particles are born assuming a Chabrier initial mass function (Chabrier 2003), with their subsequent stellar evolution and feedback implemented following the prescriptions described in Pillepich et al. (2018a).

2.2. Simulated galaxies

Galaxy catalogues are generated using the friends-of-friends (FoF, Davis et al. 1985) and SUBFIND algorithms (Springel et al. 2001; Dolag et al. 2009), respectively. We also make use the merger tree obtained with the SUBLINK algorithm (Rodríguez-Gomez et al. 2015) to track the temporal evolution of galaxies.

We restrict our analysis only to isolated galaxies (i.e., central galaxies of their own FoF group) with stellar mass $8 < \log(M_*/M_\odot) < 11$. We remove ongoing mergers by excluding galaxies with a satellite of stellar mass higher than 10% of its central host. We also exclude backsplash systems which, at some point in their evolution, were part of a massive group or cluster.

We compute galaxy properties, such as stellar mass and size, by defining as a galaxy all particles/cells within $r_{\text{glx}} = 0.15 r_{200}$ of the halo centre, where r_{200} is the virial⁴ radius.

2.3. Galaxy kinematic morphology

The morphology of a simulated galaxy can be quantified using the kinematics of its stellar component. We use the fraction of kinetic energy invested in ordered rotation, κ_{rot} (Sales et al. 2012), as an estimate of rotational support, defined as follows:

$$\kappa_{\text{rot}} = \frac{K_{\text{rot}}}{K} = \frac{1}{K} \sum \frac{1}{2} m \left(\frac{j_z}{R} \right)^2 \quad (1)$$

where $K = \sum m|v|^2/2$ is the sum of the kinetic energy of all stellar particles of the galaxy; j_z is a star particle’s specific angular momentum component perpendicular to the disc plane⁵ and R its cylindrical galactocentric distance.

As shown in Sales et al. (2012), this estimator strongly correlates with the fraction of stars with high orbital circularity parameter $\epsilon_j = j_z/j_{\text{circ}}(E)$ (Abadi et al. 2003); higher values of κ_{rot} are associated with a more prominent disc-like component. An arbitrary threshold value of $\kappa_{\text{rot}} = 0.5$ is often used to distinguish rotation-dominated galaxies from dispersion-dominated ones (see e.g. Rodríguez-Gomez et al. 2017; Du et al. 2021, 2022).

3. Results

3.1. Morphological components

As illustrative examples, we show in Figure 1 face-on and edge-on projections of the stellar (upper panels) and gaseous (lower

⁴ Throughout this paper, virial quantities are defined at the radius enclosing 200 times the critical density for closure.

⁵ We define the disc plane of a galaxy using the angular momentum of their young stars, with ages less than 1 Gyr.

³ <https://www.tng-project.org/>

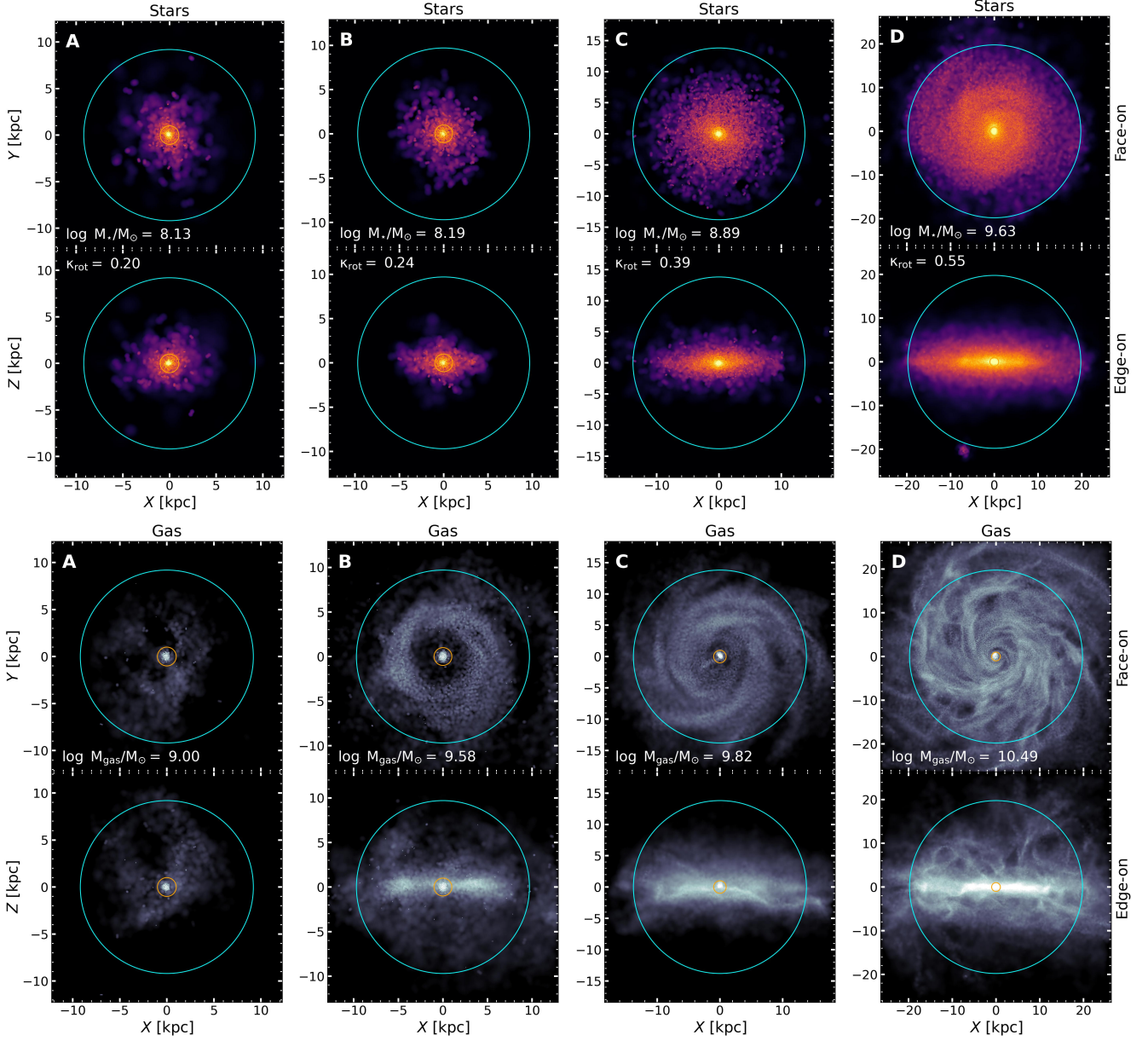


Fig. 1. Face-on and edge-on projections of stars (top panels) and gas (bottom panels) in four TNG50 central galaxies with varying stellar mass and rotational support. From left to right, galaxies increase in total stellar mass M_* , total gas mass M_{gas} and rotational support κ_{rot} (values are shown in white labels). Cyan circles indicate our definition of galaxy size $r_{\text{glx}} = 0.15 r_{200}$; orange circles mark $r = 1$ kpc. Extended gaseous and stellar discs are more clearly evident in the two most massive galaxies (C and D). All galaxies exhibit a dense baryonic clump (gas and stars) in the central regions of size $r \sim 1$ kpc. The TNG50 Subhalo_ID for these galaxies are: 830875 (A), 792447 (B), 733632 (C) and 643257 (D). Brighter colours indicate higher number density of particles. Images generated with PySPHViewer (Benítez-Llambay 2017).

panels) components of four isolated TNG50 galaxies at redshift $z = 0$. These galaxies were chosen to have κ_{rot} close to the median value at given stellar mass (see Section 3.2). Stellar mass (and κ_{rot}) increases from left to right (galaxies A, B, C and D, respectively). We indicate in each panel both $r_{\text{glx}} = 0.15 r_{200}$ (cyan circle) and $r = 1$ kpc (orange circle). The former effectively defines the central galaxy as adopted throughout this work; the latter is a fixed physical radius that encloses a dense central baryonic clump found in the innermost region of most TNG50 galaxies at $z = 0$. The total stellar mass, total gas mass and κ_{rot} of each galaxy are shown in the labels of Figure 1.

As anticipated, low values of κ_{rot} denote amorphous stellar morphologies without a well-defined disc. High values of κ_{rot} , on

the other hand, indicate systems where a co-planar, rotationally supported disc of stars dominates the morphology of a galaxy.

The spatial distribution of the gas is particularly revealing, especially when seen face-on. Three different regions can be clearly distinguished: (i) a dense ~ 1 kpc inner clump at the centre; (ii) a flattened and extended outer disc-like component; and (iii) a gap between clump and disc. These morphological components are clearly delineated in the gas component of each of these galaxies, and are surrounded by a more tenuous, irregularly-shaped gaseous envelope.

Although these gas components can be seen in all four galaxies, their relative prominence varies from galaxy to galaxy. As expected from the values of κ_{rot} , the disc component grows in importance with increasing stellar mass, from practically non-

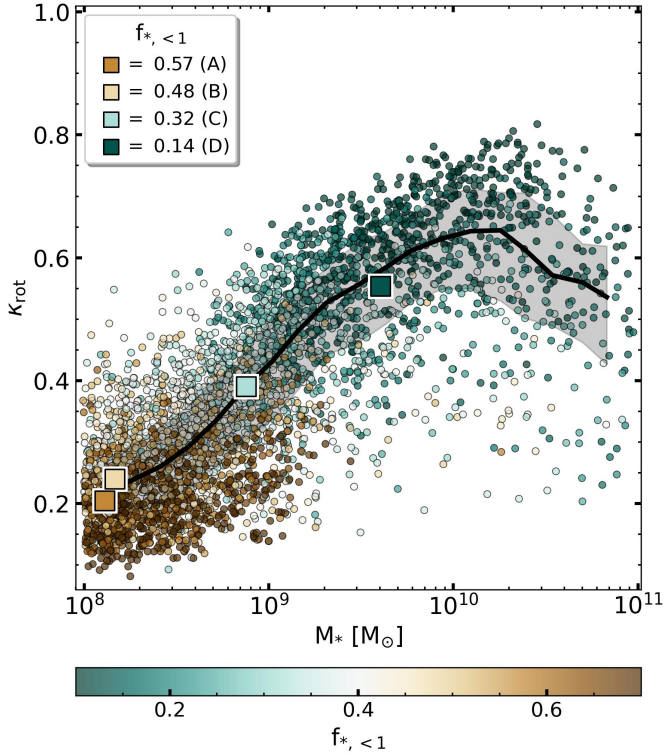


Fig. 2. Galaxy morphology estimator κ_{rot} as function of stellar mass for 3824 isolated galaxies from TNG50. Each galaxy is represented with a circle coloured by the fraction of stellar mass enclosed within 1 kpc of its centre $f_{*, <1} = M_{*, <1}/M_*$. With a black solid line and shaded region we indicate the median and the 25th-75th percentiles. Filled squares highlight the four example galaxies (A, B, C and D) shown in Fig. 1. Ordered rotation increases monotonically with stellar mass in the range $8.0 < \log(M_*/M_\odot) \leq 10.3$, with dwarf galaxies having typically $\kappa_{\text{rot}} \lesssim 0.4$. The colour gradient shows that inner regions become more dominant at lower stellar masses, reaching $f_{*, <1} > 0.5$, and these galaxies exhibit the lowest rotational support of the sample. At fixed stellar mass, κ_{rot} is anti-correlated with the stellar mass fraction in the inner regions $f_{*, <1}$.

existent in galaxy A, to clearly dominant in galaxy D. On the other hand, the central clump is seen to have similar size in all galaxies, regardless of mass, while the gap between clump and disc is particularly obvious in galaxy B. These trends suggest a close link between the spatial distribution of the gas and the morphology/rotational support of a galaxy, as we discuss next.

3.2. Rotational support vs galaxy stellar mass

We begin by exploring the galaxy mass dependence of the rotational support of the stellar component, shown in Figure 2. Here, each galaxy is represented with a circle, coloured by the fraction of its stellar mass enclosed within 1 kpc from the centre ($f_{*, <1} = M_{*, <1}/M_*$), or, in other words, by the mass fraction attached to the dense inner clump discussed in the previous subsection. The solid black line and the shaded regions indicate the median trend, as well as the 25th and 75th percentiles. The coloured squares correspond to the four example galaxies shown in Figure 1 (galaxies A, B, C and D).

This figure shows a strong positive correlation between κ_{rot} and M_* , except for the most massive galaxies (i.e., $\log(M_*/M_\odot) > 10.3$) where there is a hint of a decrease in κ_{rot} with further increases in M_* . This change in trend is driven by the

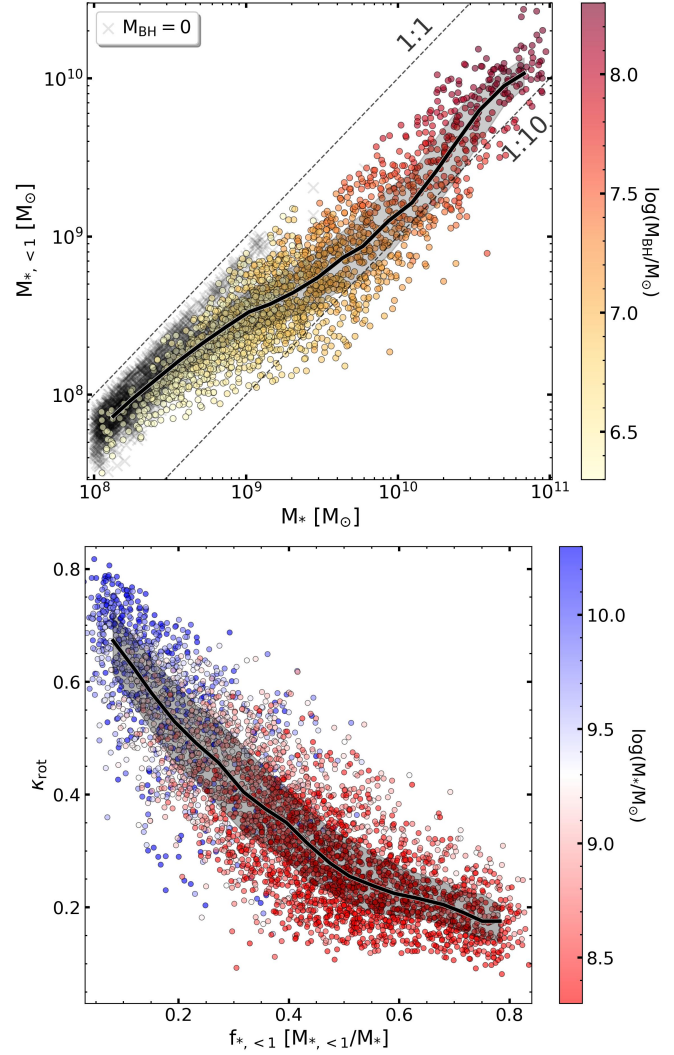


Fig. 3. *Top panel:* Stellar mass enclosed within 1 kpc of the galaxy centre ($M_{*, <1}$) as a function of total stellar mass (M_*), coloured by the central black hole mass. In the dwarf regime, most galaxies do not harbour a central massive black hole due to the seeding procedure of TNG50, and we identified them with grey crosses. Grey dashed lines show the 1:1 and 1:10 ratios, indicating that low-mass galaxies have most of their stellar mass enclosed within 1 kpc, while at higher masses the inner region represent roughly 0.1-0.2 of the total mass. *Bottom panel:* Galaxy morphology parameter κ_{rot} as function of the enclosed stellar mass fraction $f_{*, <1}$, coloured by total stellar mass. Black solid lines and shaded regions indicate the median and the 25th-75th percentiles. At low stellar masses (redder colours), the inner regions become more dominant. Rotational support is anticorrelated with the fraction of stellar mass in the inner regions.

increasing importance of late major mergers in shaping the most massive galaxies, and by the effects of the energetic feedback from Active Galactic Nuclei (AGN, see e.g. Naab et al. 2014; Genel et al. 2015; Rodriguez-Gomez et al. 2017; Sotillo-Ramos et al. 2022).

The main takeaway point of Figure 2 is, however, the strong stellar mass dependence of galaxy morphology, as measured by κ_{rot} . Broadly speaking, most, if not all, dwarf (i.e., $\log(M_*/M_\odot) < 9.0$) galaxies in TNG50 are dominated by a non-rotating spheroidal component, whereas the majority of massive galaxies have rotationally-supported discs.

The origin of this trend is not immediately obvious. One may posit, for example, that gaseous star-forming discs are unable to form in dwarfs, and that stars in dwarfs perhaps form in dense clouds before the gas has a chance to coalesce onto a disc. Galaxy B, however, provides a clear counterexample; this system has a distinctive star-forming gaseous disc but, yet, the stellar component, taken as a whole, barely rotates (i.e., $\kappa_{\text{rot}} = 0.24$).

In other words, gaseous discs do form in TNG50 dwarfs, but somehow this does not lead to prominent stellar discs, as in more massive systems. Why is then disc formation less efficient in dwarfs? Galaxy A hints at an answer. There is very little gas in this galaxy outside the inner clump, and the morphology of that gas suggests that it is disturbed and out of equilibrium.

Closer examination shows that the outer disc in Galaxy A has indeed been disturbed by feedback energy from young stars in the inner clump, which, because of the decoupled-wind⁶ strategy adopted in TNG50, is dumped outside the clump. This feedback energy is important enough to blow a gap between gas in the inner clump and outer disc in more massive galaxies (see; e.g., galaxy B or C), but in dwarfs, where discs tend to be smaller, feedback acts to disrupt incipient discs.

As a consequence, most stars in dwarfs form in the non-rotating inner clump, leading to compact systems with little rotational support. Discs tend to be more resilient in more massive systems because those discs are more extended and massive, so that the "gaps" blown by feedback from the inner clump have limited, or little, effect overall.

Further evidence for this interpretation may be found in the strong correlation between $f_{*, < 1}$ and κ_{rot} that may be gleaned from Figure 2, and which is shown in the bottom panel of Figure 3. Clearly, the higher the importance of the inner clump, the lower the rotational support of the galaxy. Since galaxy mass correlates strongly with $f_{*, < 1}$, then rotational support correlates strongly with M_* . Indeed, as shown in the top panel of Figure 3, $f_{*, < 1}$ correlates inversely with M_* , varying from roughly unity at the low mass end to 0.1-0.2 at the massive end.

The importance of the central clump as a function of M_* is clearly shown in the top panel of Figure 3. Simulated galaxies here are shown coloured by the mass of the central black hole (M_{BH}), which increases with increasing M_* . At fixed stellar mass, galaxies with higher M_{BH} tend to have higher stellar mass enclosed within 1 kpc ($M_{*, < 1}$), although the mass of the central black hole makes up typically a negligible fraction ($\sim 0.1\%$) of M_* . Most TNG50 dwarfs have no central black hole, and are shown with small grey crosses. We conclude that black holes do not play a significant role in the galaxy mass-morphology relation shown in Fig. 2.

The picture that emerges is, thus, one where the importance of the inner clump is the key ingredient that determines the rotational support of the stellar component of a TNG50 galaxy. In dwarfs, star formation proceeds mainly or solely in the inner, non-rotating clump, whose feedback, in turn, effectively prevents outer gaseous discs from forming. In more massive systems, the

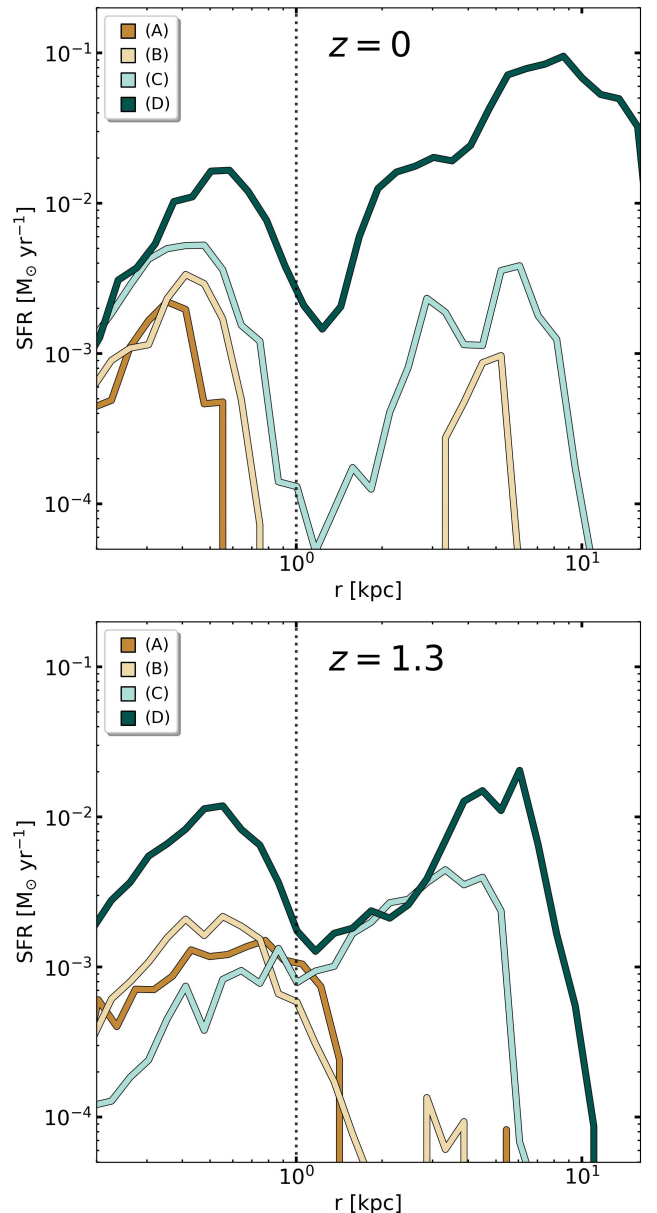


Fig. 4. Star formation rate (SFR) profiles for the example galaxies (A, B, C, and D) from Section 2 at $z = 0$ (cosmic time $t = 13.8$ Gyr, top panel) and at $z = 1.3$ ($t = 4.8$ Gyr, bottom panel). Colours are as for the squares in Figure 2: from brown for galaxy A (lowest stellar mass and κ_{rot}) to green for galaxy D (highest mass and rotational support). In the presence of a star-forming inner clump, the profiles show a relatively quiescent zone between $1 \lesssim r/\text{kpc} \lesssim 2$ that separate the central region with the outer gaseous disc. The latter is more extended and more star-forming at higher masses, while the size of the unresolved clump evolves slightly. With a grey vertical dashed line we indicate a galactocentric distance of $r = 1$ kpc, encompassing most inner star formation.

⁶ Whenever star formation occurs, stellar feedback is implemented as supernova events that create wind particles. These receive an initial wind velocity and are temporarily decoupled from the magnetohydrodynamic equations until one of the following conditions is met: i) A time of $\Delta t = 0.025 t_{\text{Hubble}}$ has elapsed (where t_{Hubble} is the age of the Universe when the star formation occurs); or ii) the wind particle reached a gas cell with a density $\rho_{\text{cell}} \leq 5\%$ of the density threshold for star formation. In TNG50, condition ii) is almost always met first (for a more comprehensive analysis of the model, see Vogelsberger et al. 2013; Pillepich et al. 2018a).

importance of the inner clump decreases, and the outer disc component is able to grow and dominate the galaxy's morphology.

Critical to this interpretation is that the size of the inner clump should be roughly independent of galaxy mass, which would explain why it becomes less and less important in more extended (massive) systems. We explore this issue next.

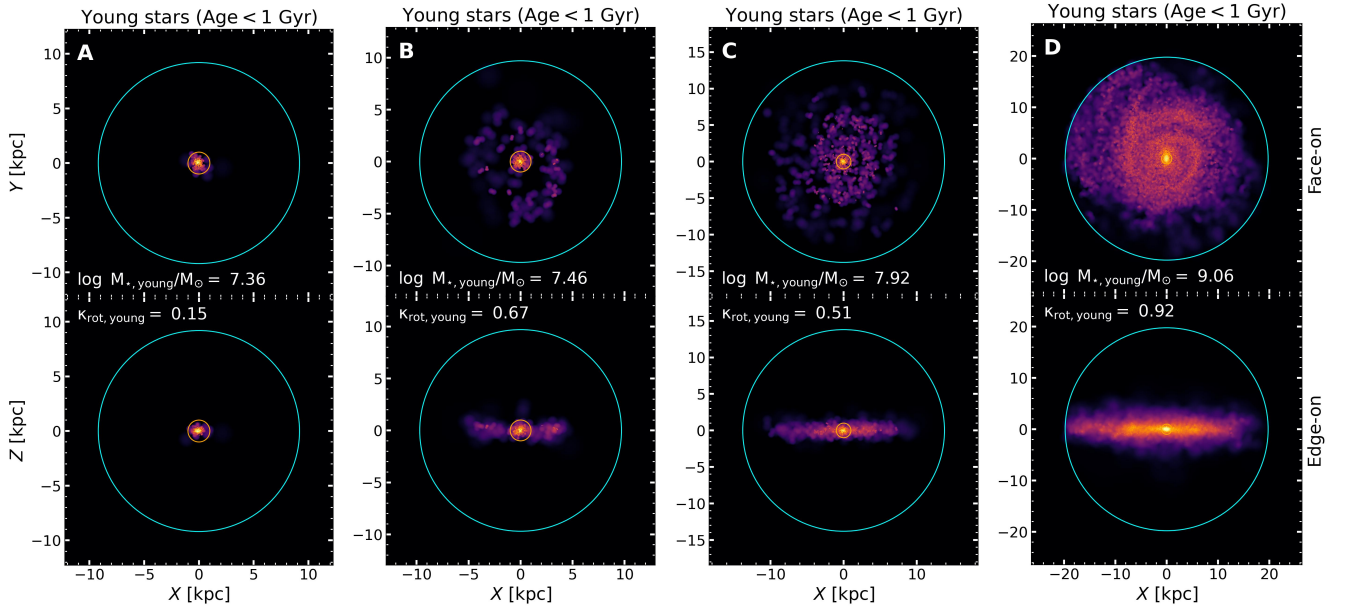


Fig. 5. Face-on and edge-on projections of young stars (defined as those with age < 1 Gyr at redshift $z = 0$) in the four illustrative examples shown in Fig. 1 (from left to right, galaxies A, B, C and D). White labels indicate the mass and rotational support of the young stellar component for each galaxy ($M_{*,\text{young}}$ and $\kappa_{\text{rot},\text{young}}$, respectively). Cyan circles show the galaxy size $r = r_{\text{glx}}$, and orange circles mark $r = 1$ kpc. All galaxies exhibit a dense young stellar component at $r < 1$ kpc, with more extended thin discs appearing in the higher-mass galaxies. Images generated with PySPHViewer (Benítez-Llambay 2017).

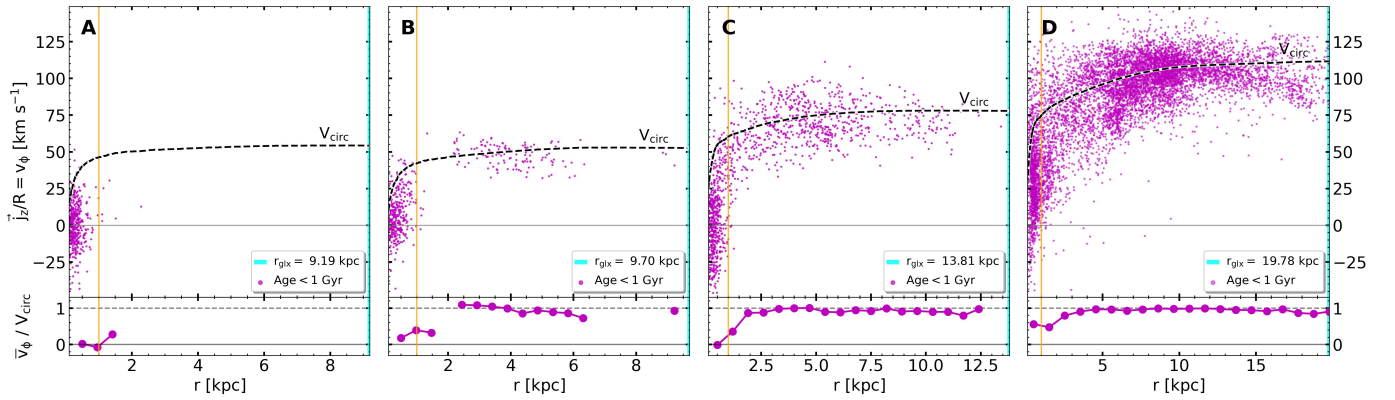


Fig. 6. Rotation velocity $v_\phi = j_z/R$ of young stars (i.e., ages < 1 Gyr, magenta dots) and circular velocity $V_{\text{circ}} = \sqrt{GM(< r)/r}$ (black dashed lines) for the four example galaxies (A, B, C and D) from Fig. 1. Bottom panels show the ratio v_ϕ/V_{circ} (magenta solid line with circles) as a function of galactocentric distance. Except for the least massive galaxy (A), all have young stars in highly circular orbits at radii $r \gtrsim 2$ kpc. Conversely, stellar particles with low tangential velocities are found in the inner regions ($r < 1$ kpc). As previously shown, higher-mass galaxies have more stars born in the outer regions.

3.3. Star formation radial profiles

Figure 4 shows the star formation rate (SFR) radial profile⁷ for the four example galaxies presented in Figure 1. Lines are colour-coded for each galaxy as in Figure 2. The top panel shows the four SFR profiles at $z = 0$, whereas the bottom panel is analogous to the top, but for $z = 1.3$.

Note that the three morphological features of the gas distribution discussed above are clearly reflected here. All four galaxies have a star-forming inner clump of size ~ 1 kpc, independent of galaxy mass, and an outer star-forming disc (except for galaxy A, where the outer disc is not forming stars at $z = 0$). The clump size does not seem to evolve with time; indeed, it is roughly 1 kpc in radius in all four galaxies at $z = 1.3$ (bottom panel in

Figure 4). Only galaxy B has a less well-defined inner clump at $z = 1.3$, suggesting that the clump is a feature that grows more massive and more clearly defined with time. The inner clump and the outer disc are separated by a gap driven by the feedback energy of young stars in the inner clump, as we discuss below in Section 3.5.

3.4. Rotational support of young stars

The gas morphology of the four example galaxies shown in Figure 1 suggests that young stars which form outside of the central clump do so in rotationally-supported discs. This is shown more clearly in Figure 5, where we plot face-on and edge-on projections of the young stars (i.e., younger than 1 Gyr) of the four galaxies at $z = 0$.

⁷ We measure the total SFR in each of 40 log-spaced radial shells between 0.06 and 25 kpc.

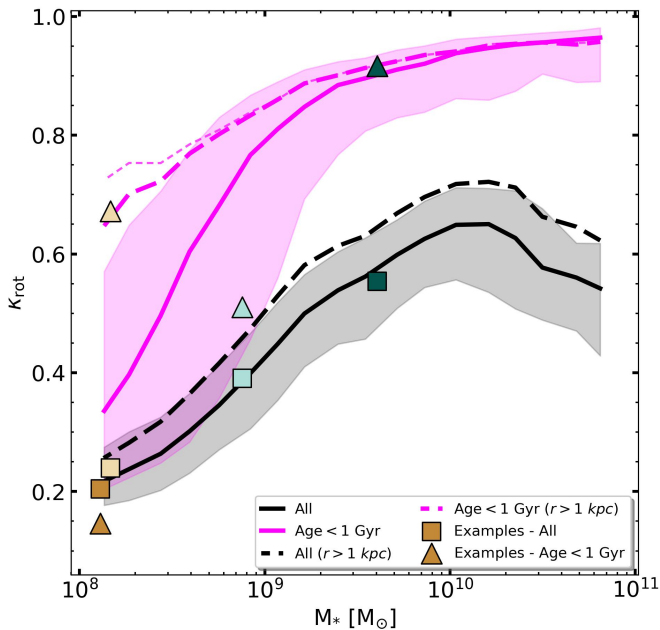


Fig. 7. Rotational support parameter κ_{rot} as a function of galaxy stellar mass. Solid and dashed lines show results for stars within the galactic radius ($r < r_{\text{glx}} = 0.15 r_{200}$) and in the outer regions ($r > 1$ kpc), respectively. Black lines represent all stars, while magenta lines represent young stars (i.e., age < 1 Gyr). Young stars in the outer regions (magenta dashed line) have $\kappa_{\text{rot}} > 0.7$, and tend to be rotation-supported in all galaxies. Conversely, young stars as a whole (magenta solid line) are non-rotating at low masses ($\kappa_{\text{rot}} < 0.5$), because in these systems most stars form in the central, non-rotating clump. Symbols correspond to galaxies A, B, C, and D, identified by colour (as in Figure 2; squares: κ_{rot} , triangles: $\kappa_{\text{rot,young}}$). A thinner magenta line indicates results when only galaxies with at least 50 young stars in the outer regions are included in the analysis.

These examples illustrate that, outside the central clump, stars form in discs, confirming the interpretation that the low values of κ_{rot} in dwarf galaxies result not because gaseous discs cannot form in such systems, but, rather, because in those systems the majority of stars form in the non-rotating central clump. The case of galaxy A also suggests that outer star-forming discs may be short-lived in dwarfs, and easily disrupted by feedback from the inner clump.

This interpretation is consistent with the kinematics of young stars in the four example galaxies, as shown in Fig. 6, where we plot the tangential velocity $v_\phi = j_z/R$ of all young stars (purple circles). The circular velocity $V_{\text{circ}} = \sqrt{GM(< r)/r}$ is also shown with a black dashed line. The bottom panels show the radial profile of the median v_ϕ , in units of the circular velocity. This figure makes clear that young stars born in the inner clump exhibit negligible rotation, while those in the outer regions show tangential velocities generally consistent with the circular velocity, albeit with considerable scatter.

Figure 7 shows that the results discussed above for the four example galaxies actually apply to the whole TNG50 galaxy population. This figure shows κ_{rot} vs M_* and is analogous to Figure 2, but splitting stars into components according to age and radius. Solid lines (and shaded areas) refer to the full TNG50 galaxy population. Black denotes using all stars in each galaxy, whereas magenta restricts the computation to only stars younger than 1 Gyr. Dashed lines correspond to stars outside the inner clump, i.e., $r > 1$ kpc. The difference between solid and

dashed magenta curves confirms that young stars outside the inner clump form in roughly rotationally-supported structures.

Such stars, however, make up a minority of all young stars in dwarfs, which are heavily dominated by the inner clump. As a result, ordered rotation is negligible in most dwarfs. One may worry that there are too few young stars with $r > 1$ kpc to compute $\kappa_{\text{rot,young}}$ reliably at the faint end. The thin dashed magenta line of Figure 7 shows results using only galaxies with a minimum of 50 young stars in the outer regions, and confirms that young stars in the outer regions are indeed formed in rotationally-supported structures.

3.5. Inner clump structure and evolution

It is clear from the above discussion that the present-day morphology of TNG50 galaxies, and dwarfs in particular, is critically dependent on the structure of the inner clump. Therefore, it is important to understand the structure of the clump and its evolution. Figure 8 shows, as a scatter plot, the radial velocity of gas cells and star particles as a function of radius for galaxies B and C, chosen as illustrative examples.

In this figure, radial velocity profiles are shown for gas (in blue) and stars (in red) in the left panels, whereas gas density profiles are shown as scatter plots in the right-hand panels. The horizontal lines indicate the threshold density for star formation (thin solid black, $\rho_{\text{min,SF}}$) as well as the density where feedback-driven winds are allowed to re-couple with the interstellar medium ($\rho_{\text{w,rec}} = 0.05 \times \rho_{\text{min,SF}}$), thick dashed line).

Inside ~ 1 kpc, the gas is dense enough to be star-forming, and appears to be near hydrostatic equilibrium (that is, almost at rest and pressure-supported), except for hints of ongoing accretion at the clump's edge. On the other hand, stars are supported by their random motions. The stellar radial velocity dispersion is shown, as a function of radius, by the dashed red curve in Figure 8. As shown in the previous subsection for young stars, there is no detectable rotational support for gas in the inner clump.

The inner clump, gap, and outer disc are clearly noticeable in this panel. The coincidence between the gas density just outside ~ 1 kpc and the wind recoupling density clearly suggests that it is feedback energy from star formation in the inner clump that carves the gap between inner clump and outer disc. These winds are responsible for the gap, and may also lead to the full disruption of the outer disc in galaxies where the disc has a size comparable to the gap, as is the case for the smallest galaxies in our sample.

We track the inner clump evolution for the whole galaxy population using the simulation's SUBLINK merger trees. We follow the main progenitors of each galaxy through cosmic time in the range $1.5 \lesssim t/\text{Gyr} \lesssim 13.8$ (corresponding to the redshift interval $4 \gtrsim z \gtrsim 0$), and measure the gas and stellar mass of their inner clump, defined at all times as simply the region enclosed within $r = 1$ (physical) kpc.

We then group galaxies by their $z = 0$ stellar mass, stacking them in 0.5 dex bins. The curves in Figure 9 show the evolution of the median enclosed stellar (dashed) and baryonic (solid) mass of the inner clumps. Lower-mass bins are shown in redder colours and higher-mass bins in bluer, with coloured circles at $t \approx 13.5$ Gyr indicating the median stellar mass M_* of each bin.

In massive galaxies, the inner clump grows quickly and stagnates relatively early so that, by $z = 0$, the clump has transformed essentially all of its baryons into stars. On the other hand, in dwarfs, the clump seems to accrete baryonic mass more continuously. These baryons are transformed less efficiently into stars,

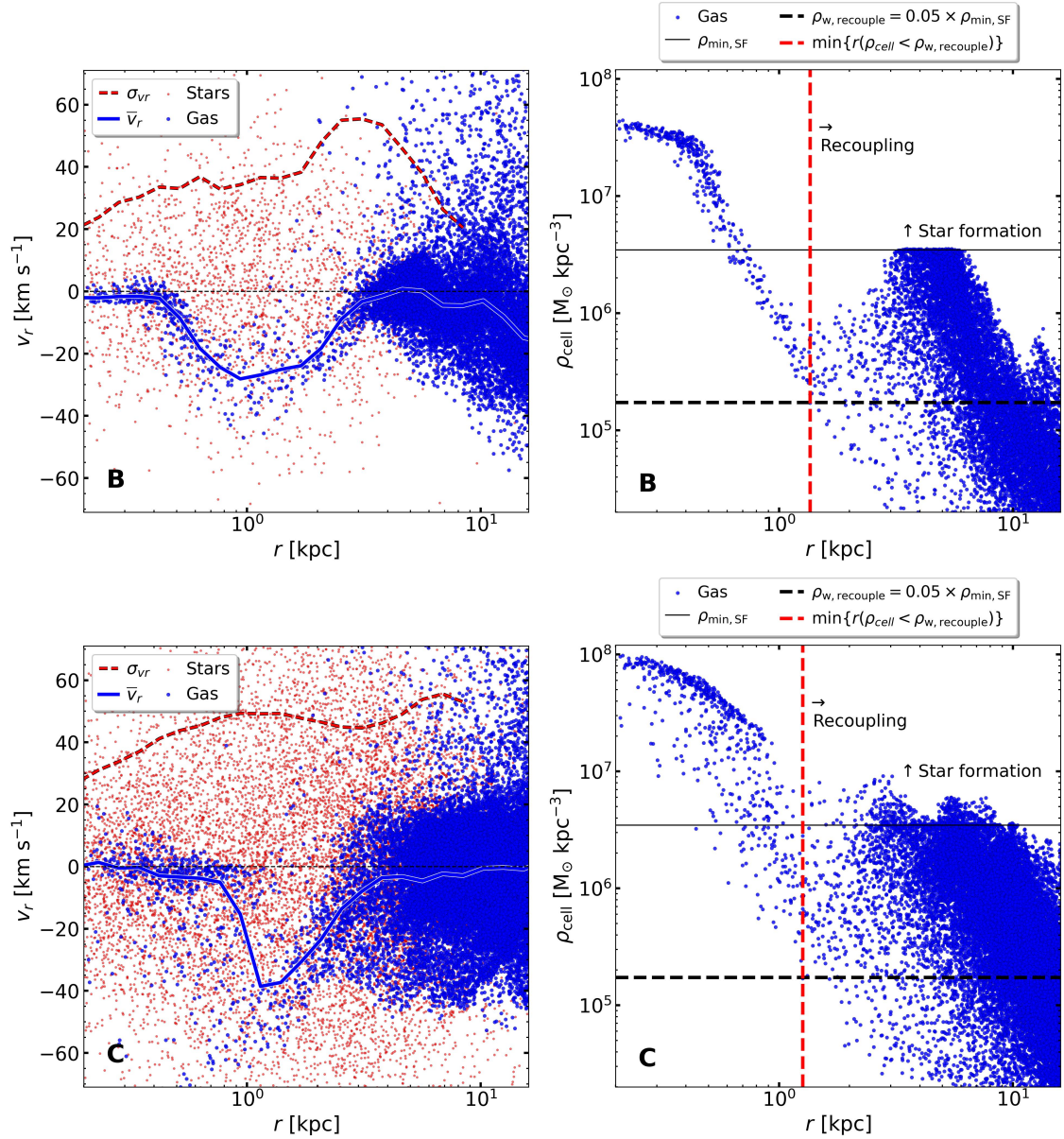


Fig. 8. *Left panels:* Radial velocity of stars (red) and gas (blue) for galaxies B and C at redshift $z = 0$, chosen as illustrative examples. The blue solid curve indicates the median radial velocity of gas cells at given radius; the red dashed curve indicates the radial velocity dispersion of star particles. *Right panels:* Gas cell density versus galactocentric distance. The horizontal solid black line shows the density threshold for star formation ($\rho_{\text{min,SF}} \approx 3.5 \times 10^6 M_{\odot} \text{ kpc}^{-3}$). The horizontal dashed line indicates the minimum wind-recoupling density, defined as $\rho_{\text{w,recouple}} = 0.05 \times \rho_{\text{min,SF}}$. The minimum radius where recoupling may occur (i.e., where a gas cell falls below $\rho_{\text{w,recouple}}$) is indicated with a vertical dashed red line. Note that the quiescent zone between the inner clump and the outer disc roughly coincides with the "recoupling radius", indicating that the star formation gap is caused by feedback winds.

so that, at $z = 0$, nearly half of the inner baryonic mass is in the form of gas.

The relative importance of the inner clump also evolves differently depending on galaxy mass, as shown in the left-hand panel of Figure 10. The clump's relative importance decreases with time in massive galaxies and increases in dwarfs. This has a knock-on effect on the evolution of galaxy sizes (middle panel of the same figure). Massive galaxies get larger with time, as young stars form progressively at larger radii, whereas star formation in dwarfs moves inward with time, as the inner clump becomes more dominant.

The effect is even more pronounced when tracking only "young stars" (i.e., those younger than 1 Gyr at any given time),

as shown in the right-hand panel of Figure 10. Interestingly, in dwarfs, the radius that contains half of young stars moves inwards: as more of the inner clump's gas is transformed into stars the star-forming region inside the clump shrinks, leading to the formation of compact stellar cores which, in some cases, can dominate the stellar population of a galaxy.

Since star formation occurs only in the central clump or in an outer gaseous disc, the size of the young stellar component is determined by the relative prevalence of these two regions. For example, the seemingly flat evolution shown by the $8.5 < \log(M_*/M_{\odot}) < 9.0$ (second reddest line) galaxy bin results because the central clump dominates in half of the systems,

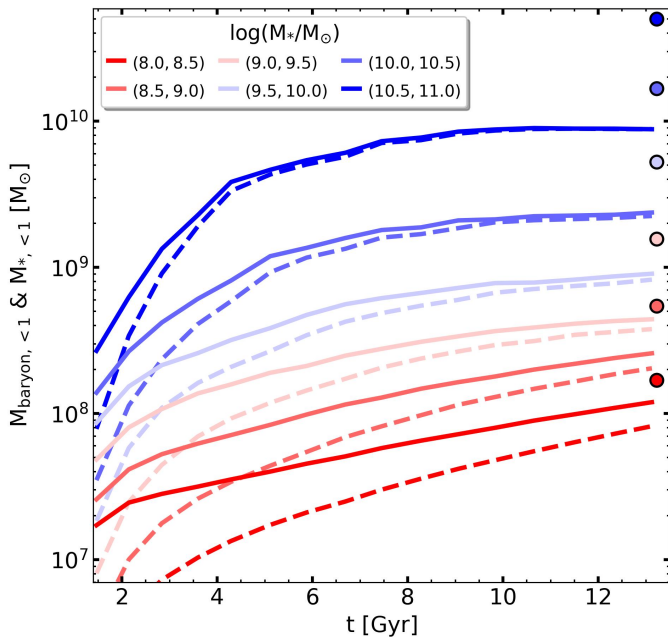


Fig. 9. Evolution of the median baryonic (solid lines) and stellar mass (dashed lines) in the inner clump (i.e., enclosed within 1 physical kpc) for stacks of galaxies in 0.5 dex M_* bins. Lines are colour coded by total stellar mass at redshift $z = 0$. The median M_* of each bin is shown by the solid circles plotted at $t \approx 13.5$ Gyr. The inner clump mass grows gradually in lower-mass galaxies (redder colours), indicating significant gas infall into their central regions and ongoing star formation. The inner clumps of more massive galaxies form early and have little gas left at $z = 0$.

whereas the outer disc dominates in the other half, roughly cancelling out the radius evolution.

The origin of the central clumps warrants further consideration. Their existence implies mechanisms capable of efficiently channelling significant amounts of gas towards the galactic centre, which may arise from a complex interplay of physical factors such as the infall of low angular momentum gas through accretion, outward angular momentum transport via non-axisymmetric structures like bars and spiral arms, or feedback-driven turbulence, as well as from numerical effects such as artificial viscosity within the gas or energy deposition of stellar feedback in the interstellar medium. Disentangling the precise contribution of each of these effects is a challenge that requires a dedicated study, which we defer to a future contribution.

3.6. Galaxy stellar mass-size relation

The relative importance of the inner clump discussed above also explains why TNG50 dwarfs have roughly the same stellar half-mass radius, $r_{50,*}$. As Figure 11 shows, the stellar half-mass radius seems to "converge" to ~ 1 kpc at low masses; intriguingly, there also appears to be a "tongue" of dwarfs with unusually low values of $r_{50,*}$, reaching values as small as 0.2 kpc (smaller than the gravitational softening length) at $\log(M_*/M_\odot) \sim 9$.

This "tongue" is made out of systems where the central clump not only dominates the stellar budget, but is also massive enough to become self-gravitating. In such systems, systems slip down the "tongue" as the gas component shrinks and is gradually transformed into stars. The colour coding in Figure 11 supports this interpretation, and shows that the "tongue" contains almost

exclusively clump-dominated systems with large values of $f_{*,<1}$. In addition, we have checked that the baryonic mass of central clumps in "tongue" systems is large enough to be comparable to (or exceed) the dark mass within 1 kpc, a feature that distinguishes them from other galaxies of comparable M_* (and larger $r_{50,*}$).

Both the flat dependence of $r_{50,*}$ at low M_* and the presence of the "tongue" are highly suggestive of an artifact caused by a combination of limited resolution as well as the particular sub-grid implementation of ISM physics and star formation/feedback in TNG50. Simple confirmation of this is provided by results from TNG100, a larger volume, lower resolution simulation that uses the same sub-grid physics implementation as TNG50. The analogous figure for TNG100 is shown in Fig. A.1. As expected from a numerically-driven feature, TNG100 galaxies show a similar flattening of the radius-mass relation at low M_* and the presence of a similar "tongue", but shifted to larger values of galaxy mass and radius.

Finally, we comment on the idea that the flattening of the $r_{50,*}$ - M_* relation may be driven by collisional effects between dark matter and stars due to the finite number of particles in low-mass systems. This was argued by Ludlow et al. (2023) to explain the resolution dependence of low-mass galaxy sizes in the EAGLE simulation series. Although these authors make a compelling case, their interpretation does not seem to apply to TNG50. In particular, the presence of a "tongue" where size decreases with increasing M_* would not be expected in such interpretation. In TNG50, at least, the flattening of $r_{50,*}$ at low M_* seems to be due to the formation of the central clump, rather than to collisional effects between dark matter and star particles.

4. Summary and Conclusions

We have used the TNG50 hydrodynamic cosmological simulation to investigate the rotational support of the stellar component of simulated galaxies. We find that the degree of rotational support (quantified by the parameter κ_{rot}) correlates strongly with galaxy stellar mass (in the range $8 < \log(M_*/M_\odot) < 11$), from mainly dispersion-dominated dwarfs to massive galaxies with prominent centrifugally supported discs.

This correlation results from the spatial distribution of gas, and, consequently, of star formation, in simulated galaxies. Star formation profiles are clearly bimodal, with an unresolved, non-rotating dense clump in the inner regions ($r < 1$ kpc), and an extended outer disc ($r > 2$ kpc). These two regions are separated by a relatively quiescent intermediate zone (a "gap"). The relative importance of one region over the other influences the morphology of a galaxy and its rotational support: in massive galaxies the inner clump is relatively unimportant and, therefore, such galaxies evolve mainly by forming stars in extended discs. On the other hand, the inner clump dominates star formation in dwarf galaxies, which, as a consequence, end up as dispersion-dominated spheroidal systems.

The gaseous inner clump is formed out of low-angular momentum, pressure-supported gas which becomes dense enough to begin forming stars. These clumps have a typical size of ~ 1 kpc, regardless of time or galaxy mass, hinting that it is an artifact of limited resolution and of the sub-grid treatment of dense gas in TNG50. The clumps are resilient to disruption, likely because the decoupled-wind feedback scheme adopted in TNG50 dumps the energetic output of young stars in the clump into its surroundings, creating the "gap" between the inner regions and the outer disc. In dwarfs, this feedback energy can disrupt the

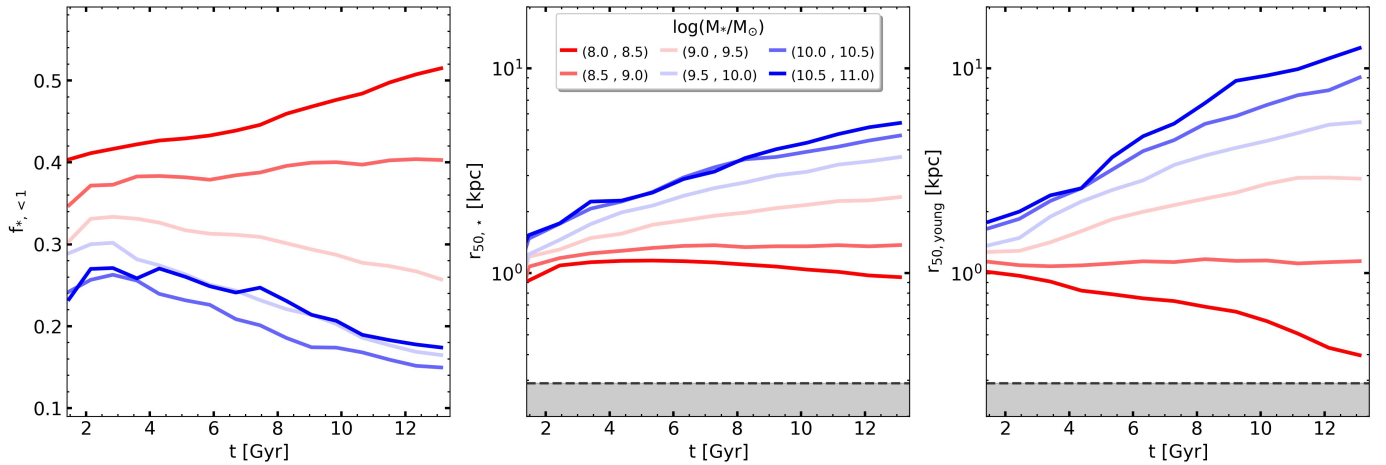


Fig. 10. Evolution of: i) the stellar mass fraction within $r < 1$ kpc, $f_{*, <1}$ (left panel); ii) the median stellar half-mass radius, $r_{50,*}$ (centre panel); and iii) the median half-mass radius of young stars (i.e., age < 1 Gyr), $r_{50,young}$ (right panel), for the same stacks of galaxies in 0.5 dex M_* bins shown in Fig. 9. Higher-mass galaxies (bluer) shows a decreasing enclosed stellar mass fraction as newly formed stars are born at progressively larger radii, consistent with *inside-out* galaxy growth. Conversely, low-mass galaxies (redder) appear to become increasingly centrally concentrated, with an *outside-in* trend where newly formed stars are found at progressively smaller galactocentric radii.

outer disc, or prevent its assembly altogether, leaving the clump as the sole, or main, dwarf galaxy star-forming region.

The relative importance of the inner clumps also has consequences regarding the galaxy mass-size relation, as well as the radial build-up of galaxies. Nearly all TNG50 dwarfs with $M_* < 10^{8.5} M_\odot$ have the same size, with stellar half-mass radii comparable to the size of the inner clump (i.e., about ~ 1 kpc). In addition, these dwarfs appear to form from the outside in, with younger stellar populations forming closer to the centre as gas in the inner clump is gradually transformed into stars.

On the other hand, the size of massive galaxies, where the inner clump prevalence is less important, or negligible, grows with increasing mass. As a consequence, massive TNG50 galaxies appear to form from the inside out, as star formation moves outward in the centrifugally supported outer discs that dominate their morphology.

Our results suggest caution when interpreting the evolution of the mass, size, and morphology of the TNG50 galaxy population, especially when using samples that contain a substantial fraction of dwarfs. The highly concentrated, unresolved baryonic clumps located at the centre of TNG50 galaxies are most likely an artifact of limited resolution and of the particular numerical implementation of star formation adopted in these simulations, which future improvements should take care to correct. Questions regarding what sets the morphology and rotational support of a galaxy, and dwarfs in particular, will probably have to wait until such improvements become available before they can be answered conclusively.

Acknowledgements. This project has received funding from the European Union's HORIZON-MSCA-2021-SE-01 Research and Innovation programme under the Marie Skłodowska-Curie grant agreement number 101086388 - Project acronym: LACEGAL. This work was partially supported by the Consejo de Investigaciones Científicas y Técnicas de la República Argentina (CONICET) and the Secretaría de Ciencia y Técnica de la Universidad Nacional de Córdoba (SeCyT). The IllustrisTNG simulations were undertaken with compute time awarded by the Gauss Centre for Supercomputing (GCS) under GCS Large-Scale Projects GCS-ILLU and GCS-DWAR on the GCS share of the supercomputer Hazel Hen at the High Performance Computing Center Stuttgart (HLRS), as well as on the machines of the Max Planck Computing and Data Facility (MPCDF) in Garching, Germany. JFN acknowledges the hospitality of the Max-Planck Institute for Astrophysics and of the Donostia International Physics Center during the completion of this manuscript.

References

- Abadi, M. G., Navarro, J. F., Steinmetz, M., & Eke, V. R. 2003, *ApJ*, 597, 21
 Adams, J. J., Simon, J. D., Fabricius, M. H., et al. 2014, *ApJ*, 789, 63
 Albers, S. M., Weisz, D. R., Cole, A. A., et al. 2019, *MNRAS*, 490, 5538
 Baldry, I. K., Driver, S. P., Loveday, J., et al. 2012, *MNRAS*, 421, 621
 Behroozi, P., Wechsler, R. H., Hearin, A. P., & Conroy, C. 2019, *MNRAS*, 488, 3143
 Benítez-Llambay, A. 2017, *Py-SPHViewer: Cosmological simulations using Smoothed Particle Hydrodynamics*, Astrophysics Source Code Library, record ascl:1712.003
 Benítez-Llambay, A., Navarro, J. F., Abadi, M. G., et al. 2016, *MNRAS*, 456, 1185
 Blanton, M. R., Lupton, R. H., Schlegel, D. J., et al. 2005, *ApJ*, 631, 208
 Chabrier, G. 2003, *PASP*, 115, 763
 Cheng, Z., Li, C., Li, N., Yan, R., & Mo, H. 2024, *ApJ*, 961, 216
 Christensen, C. R., Davé, R., Governato, F., et al. 2016, *ApJ*, 824, 57
 Davis, M., Efstathiou, G., Frenk, C. S., & White, S. D. M. 1985, *ApJ*, 292, 371
 Dekel, A. & Woo, J. 2003, *MNRAS*, 344, 1131
 Dolag, K., Borgani, S., Murante, G., & Springel, V. 2009, *MNRAS*, 399, 497
 Driver, S. P., Hill, D. T., Kelvin, L. S., et al. 2011, *MNRAS*, 413, 971
 Du, M., Ho, L. C., Debattista, V. P., et al. 2021, *ApJ*, 919, 135
 Du, M., Ho, L. C., Yu, H.-R., & Debattista, V. P. 2022, *ApJ*, 937, L18
 El-Badry, K., Wetzel, A. R., Geha, M., et al. 2017, *ApJ*, 835, 193
 Ferrarotti, A. S. & Gail, H. P. 2006, *A&A*, 447, 553
 Fu, S. W., Weisz, D. R., Starkenburg, E., et al. 2024, *ApJ*, 975, 2
 Genel, S., Fall, S. M., Hernquist, L., et al. 2015, *ApJ*, 804, L40
 Gutcke, T. A., Pakmor, R., Naab, T., & Springel, V. 2021, *MNRAS*, 501, 5597
 Karachentsev, I. D., Makarov, D. I., & Kaisina, E. I. 2013, *AJ*, 145, 101
 Kauffmann, G., Heckman, T. M., White, S. D. M., et al. 2003, *MNRAS*, 341, 33
 Klypin, A., Karachentsev, I., Makarov, D., & Nasonova, O. 2015, *MNRAS*, 454, 1798
 Li, C. & White, S. D. M. 2009, *MNRAS*, 398, 2177
 Ludlow, A. D., Fall, S. M., Wilkinson, M. J., Schaye, J., & Obreschkow, D. 2023, *MNRAS*, 525, 5614
 Marinacci, F., Vogelsberger, M., Pakmor, R., et al. 2018, *MNRAS*, 480, 5113
 Mateo, M. L. 1998, *ARA&A*, 36, 435
 McConnachie, A. W. 2012, *AJ*, 144, 4
 McNichols, A. T., Teich, Y. G., Nims, E., et al. 2016, *ApJ*, 832, 89
 McQuinn, K. B. W., van Zee, L., & Skillman, E. D. 2019, *ApJ*, 886, 74
 Moffett, A. J., Lange, R., Driver, S. P., et al. 2016, *MNRAS*, 462, 4336
 Moster, B. P., Naab, T., & White, S. D. M. 2013, *MNRAS*, 428, 3121
 Naab, T., Oser, L., Emsellem, E., et al. 2014, *MNRAS*, 444, 3357
 Naiman, J. P., Pillepich, A., Springel, V., et al. 2018, *MNRAS*, 477, 1206
 Nelson, D., Pillepich, A., Springel, V., et al. 2019a, *MNRAS*, 490, 3234
 Nelson, D., Springel, V., Pillepich, A., et al. 2019b, *Computational Astrophysics and Cosmology*, 6, 2
 Oh, S.-H., Hunter, D. A., Brinks, E., et al. 2015, *AJ*, 149, 180
 Oman, K. A., Marasco, A., Navarro, J. F., et al. 2019, *MNRAS*, 482, 821
 Ostriker, E. C. & Kim, C.-G. 2022, *ApJ*, 936, 137
 Pakmor, R., Springel, V., Bauer, A., et al. 2016, *MNRAS*, 455, 1134
 Pillepich, A., Nelson, D., Hernquist, L., et al. 2018a, *MNRAS*, 475, 648

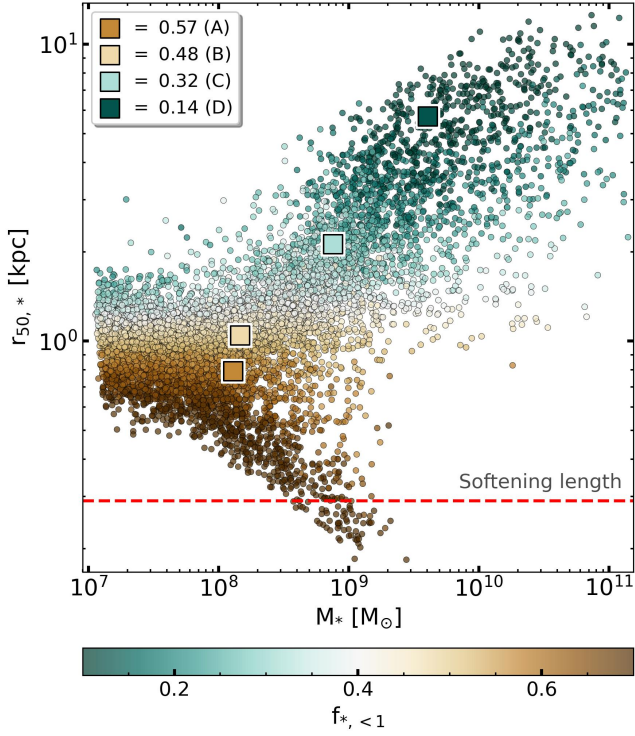


Fig. 11. Stellar half mass radius ($r_{50,*}$) as a function of stellar mass (M_*) for our sample of central TNG50 galaxies, extended to $\log(M_*/M_\odot) = 7$ (virial masses down to $\log(M_{200}/M_\odot) \sim 10$). Each galaxy is represented with a circle coloured by the fraction of stellar mass enclosed within 1 kpc of its centre $f_{*,<1} = M_{*,<1}/M_*$. Coloured squares highlight galaxies A, B, C, and D from Figure 1. We note that the stellar mass-size relation seems to "converge" to ~ 1 kpc in the dwarf regime, with a secondary population of unusually compact galaxies that reach very small $r_{50,*}$ at $\log(M_*/M_\odot) \sim 9$. These galaxies reach sizes comparable to the gravitational force softening length for stars and dark matter particles (0.29 kpc at redshift $z = 0$), and correspond to systems where the central clump dominates not only the galaxy stellar mass budget, but also the total mass budget within 1 kpc. See text for further discussion.

- Pillepich, A., Nelson, D., Springel, V., et al. 2019, MNRAS, 490, 3196
 Pillepich, A., Springel, V., Nelson, D., et al. 2018b, MNRAS, 473, 4077
 Planck Collaboration, Ade, P. A. R., Aghanim, N., et al. 2016, A&A, 594, A13
 Riggs, C. L., Brooks, A. M., Munshi, F., et al. 2024, arXiv e-prints, arXiv:2408.10379
 Rodriguez-Gomez, V., Genel, S., Vogelsberger, M., et al. 2015, MNRAS, 449, 49
 Rodriguez-Gomez, V., Sales, L. V., Genel, S., et al. 2017, MNRAS, 467, 3083
 Sales, L. V., Navarro, J. F., Theuns, T., et al. 2012, MNRAS, 423, 1544
 Sales, L. V., Wetzel, A., & Fattahi, A. 2022, Nature Astronomy, 6, 897
 Sotillo-Ramos, D., Pillepich, A., Donnari, M., et al. 2022, MNRAS, 516, 5404
 Springel, V. 2010, MNRAS, 401, 791
 Springel, V. & Hernquist, L. 2003, MNRAS, 339, 289
 Springel, V., Pakmor, R., Pillepich, A., et al. 2018, MNRAS, 475, 676
 Springel, V., White, S. D. M., Tormen, G., & Kauffmann, G. 2001, MNRAS, 328, 726
 Swaters, R. A., Sancisi, R., van Albada, T. S., & van der Hulst, J. M. 2009, A&A, 493, 871
 Tau, E. A., Vivas, A. K., & Martínez-Vázquez, C. E. 2024, AJ, 167, 57
 van den Bosch, F. C. & Swaters, R. A. 2001, MNRAS, 325, 1017
 Vogelsberger, M., Genel, S., Sijacki, D., et al. 2013, MNRAS, 436, 3031
 Vogelsberger, M., Genel, S., Springel, V., et al. 2014, Nature, 509, 177
 Walter, F., Brinks, E., de Blok, W. J. G., et al. 2008, AJ, 136, 2563
 Weinberger, R., Springel, V., Hernquist, L., et al. 2017, MNRAS, 465, 3291
 York, D. G., Adelman, J., Anderson, John E., J., et al. 2000, AJ, 120, 1579

Appendix A: Size-mass relation in TNG50 & TNG100

In Table A.1 we list numerical parameters of the TNG50-1 and TNG100-1 runs of the Illustris TNG suite (as listed in Nelson et al. 2019b). Although TNG50-1 has higher resolution than TNG100-1 (and a smaller volume) both simulations share the sub-grid physics implementation of e.g. magnetic fields, black hole accretion and feedback, wind directionality, velocity and energy and metal tagging (see Appendix A Pillepich et al. 2018b).

Table A.1. Numerical parameters for the TNG50-1 and TNG100-1 runs of the IllustrisTNG suite. From left to right: Name of the simulation, side of the cosmological box at redshift $z = 0$, mass of dark-matter particles, target-mass of stellar particles/gas cells, force softening length for dark matter and stellar particles, minimum force softening length for gas cells.

Run	L_{box} [Mpc]	m_{DM} [M_{\odot}]	m_{baryon} [M_{\odot}]	$\epsilon_{\text{DM},*}$ [kpc]	$\epsilon_{\text{gas,min}}$ [kpc]
TNG50-1	51.7	$4.5 \cdot 10^5$	$8.5 \cdot 10^4$	0.29	0.07
TNG100-1	110.7	$7.5 \cdot 10^6$	$1.4 \cdot 10^6$	0.74	0.18

The effects of unresolved baryonic clumps at the innermost regions of galaxies are likely due to the sub-grid physics implementation. In Figure A.1 we compare the size-mass relation for isolated central galaxies of TNG50-1 (left panel, as in Figure 11) and TNG100-1 (right panel). A "tongue" of galaxies that reach extremely small size can be identified in both simulations. However, the numerical feature in TNG100-1 occurs at higher stellar masses and larger sizes, a clear indication of numerical artifact.

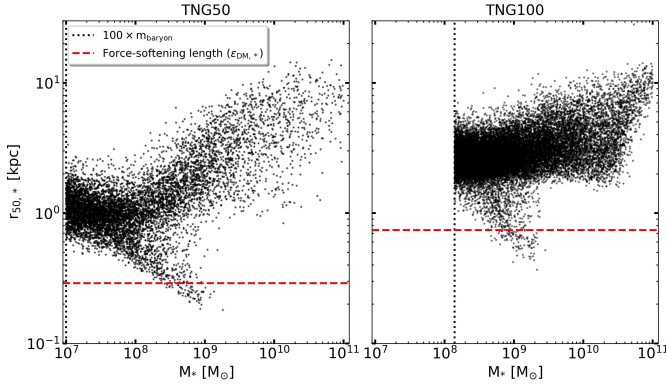


Fig. A.1. Stellar half mass radius ($r_{50,*}$) as a function of stellar mass (M_*) for all isolated central galaxies in TNG50-1 (left panel, similar to Figure 11) and in TNG100-1 (right panel). All galaxies shown have more than 100 stellar particles and more than 100 dark matter particles. Red dashed lines indicate the force softening length for dark matter and stellar particles for each simulation. The "tongue" is also present in TNG100, but at slightly higher masses and with larger size, suggesting that this feature is numerical in origin.